

Accepted for publication in ApJ, July 2 2010

Properties of the T8.5 Dwarf Wolf 940 B

S. K. Leggett¹

sleggett@gemini.edu

D. Saumon²Ben Burningham³Michael C. Cushing⁴M. S. Marley⁵

and

D. J. Pinfield³

ABSTRACT

We present 7.5–14.2 μm low-resolution spectroscopy, obtained with the *Spitzer* Infrared Spectrograph, of the T8.5 dwarf Wolf 940 B, which is a companion to an M4 dwarf with a projected separation of 400 AU. We combine these data with previously published near-infrared spectroscopy and mid-infrared photometry, to produce the spectral energy distribution for the very low-temperature T dwarf. We use atmospheric models to derive the bolometric correction and obtain a luminosity of $\log L/L_{\odot} = -6.01 \pm 0.05$ (the observed spectra make up 47% of the total flux). Evolutionary models are used with the luminosity to constrain the values of effective temperature (T_{eff}) and surface gravity, and hence

¹Gemini Observatory, Northern Operations Center, 670 N. A‘ohoku Place, Hilo, HI 96720

²Los Alamos National Laboratory, PO Box 1663, MS F663, Los Alamos, NM 87545

³Centre for Astrophysics Research, Science and Technology Research Institute, University of Hertfordshire, Hatfield AL10 9AB

⁴JPL, Department of Astrophysics, 4800 Oak Grove Drive, Pasadena, CA 91109

⁵NASA Ames Research Center, Mail Stop 245-3, Moffett Field, CA 94035

mass and age for the T dwarf. We ensure that the spectral models used to determine the bolometric correction have T_{eff} and gravity values consistent with the luminosity-implied values. We further restrict the allowed range of T_{eff} and gravity using age constraints implied by the M dwarf primary, and refine the physical properties of the T dwarf by comparison of the observed and modelled spectroscopy and photometry. This comparison indicates that Wolf 940 B has a metallicity within ~ 0.2 dex of solar, as more extreme values give poor fits to the data — lower metallicity produces a poor fit at $\lambda > 2 \mu\text{m}$ while higher metallicity produces a poor fit at $\lambda < 2 \mu\text{m}$. This is consistent with the independently derived value of $[\text{m}/\text{H}] = +0.24 \pm 0.09$ for the primary star, using the Johnson & Apps (2008) $M_K:V - K$ relationship. We find that the T dwarf atmosphere is undergoing vigorous mixing, with an eddy diffusion coefficient K_{zz} of 10^4 to $10^6 \text{ cm}^2 \text{ s}^{-1}$. We derive an effective temperature of 585 K to 625 K, and surface gravity $\log g = 4.83$ to 5.22 (cm s^{-2}), for an age range of 3 Gyr to 10 Gyr, as implied by the kinematic and $\text{H}\alpha$ properties of the M dwarf primary. Gravity and temperature are correlated such that the lower gravity corresponds to the lower temperature and younger age for the system, and the higher values to the higher temperature and older age. The mass of the T dwarf is $24 M_{\text{Jupiter}}$ to $45 M_{\text{Jupiter}}$ for the younger to older age limit.

Subject headings: stars: brown dwarfs, fundamental parameters, individual (Wolf 940 B) — infrared: stars

1. Introduction

The study of brown dwarfs, stellar-like objects with a mass below that required for the onset of hydrogen fusion (e.g. Burrows et al. 2001), has advanced dramatically in the last decade. Primarily this has been due to the discovery of a significant population of brown dwarfs by far-red and near-infrared surveys: the Sloan Digital Sky Survey (SDSS, York et al. 2000), the Two Micron All Sky Survey (2MASS, Skrutskie et al. 2006), the UK Infrared Telescope (UKIRT) Infrared Deep Sky Survey (UKIDSS, Lawrence et al. 2007) and the Canada France Hawaii Telescope’s Brown Dwarf Survey (CFBDS; Delorme et al. 2008b). The latest spectral type and coolest dwarfs currently known are classified as T dwarfs. At the time of writing there are eight objects known with type later than T8: ULAS J003402.77-005206.7 (T9, hereafter ULAS 0034-00, Warren et al. 2007), CFBDS J005910.90-011401.3 (T9, Delorme et al. 2008a), ULAS J123828.51+095351.3 and ULAS J133553.45+113005.2 (T8.5 and T9, Burningham et al. 2008), Wolf 940 B (T8.5, Burningham et al. 2009,

hereafter B09), ULAS J130217.21+130851.2 (T8.5, Burningham et al. 2010), Ross 458 C (T8.5, Goldman et al. 2010) and UGPS J072227.51-054031.2 (T10, Lucas et al. 2010). These extreme objects have very low effective temperatures (T_{eff}) of 500 – 600 K (e.g. Leggett et al. 2010), approaching the temperature where water clouds are expected to form in the atmosphere (e.g. Burrows et al. 2003).

The T dwarfs that have stellar companions are of particular interest as the primary can provide distance, metallicity and age constraints for the brown dwarf. There are ten known examples of such systems at this time. In order of increasing T dwarf sub-class they are: Gl 337 CD (T0, T0 + K1V + G9V; Wilson et al. 2001, Burgasser et al. 2005); Epsilon Indi Bab (T1, T6 + K5V; Scholz et al. 2003, McCaughrean et al. 2004); HN Peg B (T2.5 + G0V; Luhman et al. 2007, Leggett et al. 2008); SCR 1845-6357 B (T6 + M8.5; Biller et al. 2006, Kasper et al. 2007); Gl 229 B (T7p + M1V; Nakajima et al. 1995; Leggett et al. 2002); HD 3651 B (T7.5 + K0V; Mugrauer et al. 2006, Burgasser 2007, Liu et al. 2007, Luhman et al. 2007); Gl 570 D (T7.5 + M3V + M1.5V + K4V; Burgasser et al. 2000, Saumon et al. 2006, Geballe et al. 2009); Wolf 940 B (T8.5 + M4V, B09); Ross 458 C (T8.5 + M7V + M0.5; Goldman et al. 2010). The degree of accuracy that can be obtained in measurements of the fundamental parameters of such T dwarfs is illustrated by the Geballe et al. (2009) study of the T7.5 dwarf Gl 570D. The Gl 570 system has a well determined distance and metallicity, and the K4V primary constrains the age to be between 2 and 5 Gyr (Geballe et al. 2001). Comparison of the observed luminosity and spectral properties of the T dwarf to atmospheric and evolutionary models constrains T_{eff} to be 800 – 820 K and the gravity to be $\log g = 5.09 - 5.23$. These values constrain the age further to 3 to 5 Gyr, and the mass of the T dwarf to be between 38 and 47 M_{Jupiter} .

This paper presents an analysis of the spectral energy distribution (SED) of the T8.5 dwarf Wolf 940 B. The dwarf was discovered in the Large Area Survey component of the UKIDSS, and identified as a companion to the M4V star Wolf 940 (also known as LHS 3708 and GJ 1263), by B09. B09 present near-infrared spectroscopy and photometry, as well as L' photometry, for the T dwarf. They use these data to derive the luminosity of the dwarf, and hence T_{eff} and surface gravity. Leggett et al. (2010) give *Spitzer* Infrared Array Camera (IRAC, Fazio et al. 2004) [3.6], [4.5], [5.8] and [8.0] photometry for the T dwarf and use the infrared colors to support and further constrain the atmospheric properties determined by B09. Here we report new mid-infrared spectroscopy for Wolf 940 B, obtained with the *Spitzer* Infrared Spectrograph (IRS, Houck et al. 2004). The improved accuracy of the luminosity we derive, and the additional spectroscopy, enables us to refine the B09 results. Wolf 940 B is currently the coolest companion to a star with both near- and mid-infrared photometric and spectroscopic data. A more complete energy distribution for such a cool object, which has other basic data provided by its companion (distance, age and metallicity),

provides a good test of the model atmospheres for these almost-planetary objects.

In §2 we describe the Wolf 940 system. The IRS data are presented in §3. In §4 we use atmospheric and evolutionary models to calculate an accurate luminosity for Wolf 940 B, and constrain its fundamental properties. Our conclusions are given in §5.

2. The Wolf 940 System

The Wolf 940 binary consists of a widely separated M4 and T8.5 dwarf pair (Reid et al. 1995, B09). Table 1 lists the astrometric and photometric properties of the system. The primary is a high proper-motion M4 dwarf, identified in historic proper motion surveys as Wolf 940 (and LHS 3708, GJ 1263, amongst other identifiers).

B09 use the colors of the primary and the $M_K:V - K$ relationships presented by Bonfils et al. (2005) to derive a metallicity $[m/H] = -0.06 \pm 0.20$ for the system. However Leggett et al. (2010) show that the $H - K$ and $H - [4.5]$ colors of the secondary imply that the system has solar or slightly super-solar metallicity. Here we use the Johnson & Apps (2008) significant revision of the Bonfils et al. calibration, together with the parallax, V and K values given in Table 1, to derive a metallicity of $[m/H] = +0.24 \pm 0.09$ for the system. We discuss metallicity further in §4.6.

The measured radial velocity, combined with the parallax and proper motion, give UVW space motions of 35, -49 and -26 kms^{-1} (B09 and references therein), typical of old disk objects. B09 match the combination of the kinematics and the Bonfils et al. metallicity value to the 3 – 5 Gyr-old disk population in the Galaxy population synthesis model by Robin et al. (2003). In this paper we constrain the age of the system using the Geneva-Copenhagen survey of age, kinematics and metallicity of a large number of stars in the solar neighbourhood (Holmberg et al. 2009). Based on this work, the UVW velocities and revised metallicity of the Wolf 940 system implies an age of between 3 Gyr and 10 Gyr. We adopt this age range, taking a more conservative approach than B09.

Wolf 940 A shows the $H\alpha$ line in absorption, with an equivalent width of -0.26 \AA , typical for an M4 dwarf (Gizis et al. 2002, their Figure 6). The evolution of chromospheric activity in low mass stars is a complex process, and its relationship to the strength of the $H\alpha$ line is not well understood (e.g. Gizis et al. 2002, West et al. 2008, Walkowicz & Hawley 2009). While it is clear that $H\alpha$ in emission implies a highly active and therefore young star, stars with $H\alpha$ in absorption may have no to moderate activity. Given that Wolf 940 A shows the line in absorption with a very typical strength for its type, we assume that it is no longer active and is therefore older than 3 Gyr, which is the lower limit on the activity lifetime

for an M4 dwarf (West et al. 2008, their Figure 10). Again we take a more conservative approach than B09, and do not assume that the presence of $H\alpha$ absorption implies that the star is still somewhat active, and so we do not put an upper limit on the age of the system based on chromospheric activity arguments.

In summary, the kinematic and $H\alpha$ properties of Wolf 940 A imply that the system is between 3 and 10 Gyr old. A rotational velocity for Wolf 940 A would be useful as it would allow a gyrochronology age to be determined. The metallicity of the system is approximately solar.

3. Observations

We obtained *Spitzer* IRS spectra of Wolf 940 B via the Director’s Discretionary Time program 527. The Short-Low module was used in first order which provides a spectrum covering the $7.5 - 14.5 \mu\text{m}$ range, with a resolution of $R \approx 120$. A nearby star was used in the blue peak-up array to acquire the target in the $3''.7$ slit. Standard staring mode was used with a ramp duration of 60s and 84 cycles, for an observation of duration 3.6 hours; two such observations were obtained. Each cycle places the target at two slit positions, about one-third and two-thirds of the way along the slit. Thus the total on-source exposure was 5.6 hours. Both observations were carried out on the 16th December 2008.

We used the Basic Calibrated Data (BCD) produced by the *Spitzer* pipeline version S18.7.0. This produces a two-dimensional long-slit spectrum at each of the nod positions, so for each of our two observations there are 84 files for each nod position. The BCD files have been processed by the pipeline, which includes ramp fitting, dark subtraction, droop correction, linearity correction, flat fielding, and wavelength calibration (see Section 5.1 of the IRS Instrument Handbook ⁶).

We treated the two observations as independent datasets. We used the IRAF data reduction tool (Tody 1993) to subtract each nod pair, and combined the 84 subtracted images using sigma-clipping in the `imcombine` routine. Some structure remained in the background of the combined images; we removed this by subtracting a smoothed version of the image, using an 11×11 box. This residual-structure subtracted image was then fed into the *Spitzer* IRS data reduction package SPICE. ⁷ The source signal was low, and there were a large number of bad and hot pixels.

⁶<http://ssc.spitzer.caltech.edu/irs/irsinstrumenthandbook/49/>

⁷<http://ssc.spitzer.caltech.edu/dataanalysisistools/tools/spice/spiceusersguide/1/>

SPICE takes as input: the image file, a bad pixel mask and an uncertainty image. We used the sigma image produced by the `imcombine` routine as the uncertainty mask, and a bad pixel mask included with the bcd files. SPICE traces the appropriate module’s slit profile over the input image, allowing the user to set the location and the width of the extraction window. We extracted the positive and negative spectrum using a relatively small window of 2 pixels in order to avoid adding noise. The final step in the SPICE application converts the signal to a flux density.

We combined the two negative and two positive extracted spectra manually. The signal to noise is quite low ($S/N \approx 4\text{--}10$), and we visually identified bad data points by comparison of the four spectra. Figure 1 shows the final spectrum, with the noise spectrum which is based on the deviation between the four individual spectra. We checked the flux calibration by synthesizing the IRAC [8.0] photometry from the spectrum, after extending it to the short end of the filter bandpass ($\sim 6.3 \mu\text{m}$) using as a template the IRS second order spectrum of a bright T8 dwarf (this extension contributed 17% of the total flux through the filter). This check indicated that the flux calibration is good to 5%.

4. Analysis

Our analysis is based on a method we developed that uses synthetic spectra to determine a bolometric correction that is consistent with the luminosity obtained from evolution models. Because the effective temperatures and gravities obtained in this fashion are obtained from the *integrated* observed flux and not by fitting the observed spectrum, it is quite robust and is not sensitive to the known (and unknown) systematic biases that arise when fitting model spectra to the observed spectrum.

The solution for the T_{eff} and gravity is further refined by direct comparison of the corresponding synthetic spectra with the spectroscopic and photometric data, as well as age constraints. In this section, we first obtain T_{eff} and the gravity using solar metallicity models. The mid-infrared photometry and spectrum allow an exploration of non-equilibrium chemistry driven by vertical transport and we estimate the mixing time scale. Finally, we perform the analysis again with non-solar metallicity models and by considering the uncertainty in L_{bol} .

4.1. Effective Temperature and Gravity

Our analysis of Wolf 940 B is based on the atmospheric models and non-equilibrium chemistry scheme described in Saumon et al. (2006, 2007) and the evolution sequences of Saumon & Marley (2008). We use cloudless atmospheres and evolution as appropriate for a late T dwarf, and initially assume solar metallicity. The observed $1.05 - 2.43 \mu\text{m}$ spectrum (B09) and $7.5 - 14.2 \mu\text{m}$ spectrum (this work) are integrated to give an observed flux at Earth of $9.22 \pm 0.24 \times 10^{-14} \text{ erg s}^{-1} \text{ cm}^{-2}$. The IRS spectrum contributes 39% of this value. Following the method described in Geballe et al. (2001) and Saumon et al. (2006, 2007), we derive a family of (T_{eff}, g) values that provide L_{bol} values that are consistent with the bolometric correction from the model spectra and the evolution. That is, the (T_{eff}, g) of the spectral model used to calculate the correction from observed to total flux, must be consistent with the (T_{eff}, g) implied by the evolutionary models for that total luminosity. These (T_{eff}, g) solutions are shown in Figure 2 and Table 2, and correspond approximately to a constant L_{bol} curve in the (T_{eff}, g) plane. The bolometric correction amounts to $\sim 53\%$ of the luminosity, and the derived luminosity is $\log L_{\text{bol}}/L_{\odot} = -6.009$ (for $T_{\text{eff}} = 600 \text{ K}$, see below and Table 2). Combining the uncertainty in the flux calibration of the spectrum (using a Monte Carlo sampling of a Gaussian distribution of the calibration uncertainty for each segment of the spectrum) and in the distance, the uncertainty in L_{bol} is $\pm 0.047 \text{ dex}$.

Figure 2 shows evolutionary sequences in a T_{eff} against $\log g$ plot; the allowed set of values for Wolf 940 B obtained with the method outlined above is indicated by the sequence of solid dots. The T_{eff} is thus constrained to be in the range of 500 to 640 K. This range can be narrowed from a knowledge of the age of the system, or by comparison of the data to model spectra. The (T_{eff}, g) of the models used to generate the synthetic spectra for such a data comparison must fall between the dashed red lines of Figure 2, which corresponds to $\log L_{\text{bol}}/L_{\odot} = -6.009 \pm 0.047$. Figure 2 also demonstrates how each $(T_{\text{eff}}, \log g)$ pair determines the dwarf’s mass and age. Table 2 gives the set of allowed parameters (T_{eff} , $\log g$, $\log L_{\text{bol}}/L_{\odot}$, mass, radius and age) in steps of $\Delta T_{\text{eff}} = 25 \text{ K}$ for ages ranging from 0.4 to 10 Gyr and for solar metallicity. The impact of varying metallicity is discussed below in §4.6.

4.2. Comparison with the Near-Infrared Spectrum

Having constrained the allowed (T_{eff}, g) parameter range, we compare the corresponding synthetic spectra with the data. Figure 3 shows such a comparison for the solutions with ages of 1, 5.5 and 10 Gyr, i.e. the $(T_{\text{eff}}, \log g)$ solutions (575, 4.722), (600, 4.989) and (625, 5.221) (see Table 2). Note that the scaling of the model fluxes to the data is not

adjustable: it is fixed by the measured distance to the Wolf 940 system and the radius given in Table 2, determined by evolutionary models from the values of $(T_{\text{eff}}, \log g)$. Here we have assumed solar metallicity and an eddy diffusion coefficient $K_{zz} = 10^6 \text{ cm}^2 \text{ s}^{-1}$. The eddy diffusion coefficient parameterizes the time scale of vertical mixing in the upper radiative region of the atmosphere, that drives the chemistry of carbon and nitrogen out of equilibrium (Saumon et al. 2006, 2007; Hubeny & Burrows 2007). In this analysis, we have considered $K_{zz} = 0$ (chemical equilibrium), 10^2 , 10^4 and $10^6 \text{ cm}^2 \text{ s}^{-1}$. T dwarfs typically have values of K_{zz} between 10^4 and $10^6 \text{ cm}^2 \text{ s}^{-1}$ (e.g. Saumon et al. 2007, Leggett et al. 2009, Stephens et al. 2009); the effect of varying K_{zz} is discussed further below. In the deeper convection zone, the mixing time scale is determined from the mixing length formulation of convection.

As shown by Figure 3, and as we have found for other late T dwarfs, the near-infrared spectra of models constrained with our method are very nearly identical (Saumon et al. 2007, Geballe et al. 2009). Since these models have very nearly the same L_{bol} , it is a fairly accurate statement that the near infrared spectra of low- T_{eff} models are independent of gravity *at fixed* L_{bol} , for a given metallicity. This is because the effect of increasing the gravity is partially canceled by the accompanying increase in effective temperature. Also note that the effect of vertical mixing is not significant in the near-infrared at these T_{eff} (e.g. Saumon et al. 2006, and §4.4 below).

The match to the near-infrared spectrum is poor, with the modelled J and H peaks high and the K low (Figure 3, top panel). This has been noticed before and is likely due to the known incompleteness of the molecular opacity line lists in this region (e.g. Saumon & Marley 2008).

4.3. Comparison with the Mid-Infrared Spectrum

In contrast to the near-infrared region, differences are seen between the mid-infrared synthetic spectra generated by the approximately constant-luminosity models (Figure 3, lower panel). Calculation of the reduced χ^2 between the models and the observed mid-infrared spectrum shows that the best match is the $T_{\text{eff}} = 600 \text{ K}$ model ($\chi^2 = 3.64$), which is better than the 575 K ($\chi^2 = 4.93$) and 625 K ($\chi^2 = 4.29$) solutions. The $T_{\text{eff}} = 550 \text{ K}$ solution is clearly excluded with $\chi^2 = 10.7$.

Vertical transport in the convection zone drives the chemistry of nitrogen away from equilibrium and results in a typical depletion of NH_3 of a factor of 8 – 10 (e.g. Saumon et al. 2006). This increases the overall flux level in the $9 - 15 \mu\text{m}$ region where absorption by NH_3 dominates. A comparison of the observed spectrum and synthetic spectra computed

with equilibrium chemistry gives large χ^2 values — from 6.9 (550 K solution) to 11.7 (625 K solution). Those higher χ^2 values arise from the inability of the equilibrium models to match the overall flux level of the IRS spectrum for $\lambda > 9\,\mu\text{m}$ (Saumon et al. 2006, see also further discussion below). We can conclude that there is convincing evidence for a depleted abundance of NH_3 in the atmosphere of Wolf 940 B, which is consistent with findings from all of the other IRS spectra of late T dwarfs (Saumon et al. 2006, 2007; Burgasser et al. 2008, Leggett et al. 2009).

4.4. Comparison with 3 – 9 μm Photometry

Synthetic fluxes in the L' and IRAC band passes were obtained by integrating the model spectra over the filter band passes, and these are shown in Figure 3. The IRAC [3.6] photometry is not well matched by any of the models. This is a known model deficiency; Leggett et al. (2009, 2010) show that the calculated [3.6] fluxes are systematically low by 20 – 50%. It is not clear if this is related to missing opacities in the near-infrared (which may lead to too high near-infrared fluxes and too low mid-infrared fluxes), or if it is due to distortions of the pressure-temperature structure of our non-equilibrium models.

The reduced χ^2 between the synthetic and measured photometry in these five bands strongly favor the highest T_{eff} model at 625 K as well as a value of the eddy diffusion coefficient of $\log K_{zz} \approx 6$. However, the χ^2 is dominated by a large contribution from the IRAC [3.6] band pass (Figure 3). If we ignore this flux measurement, then all three models with $T_{\text{eff}} \geq 575\,\text{K}$ and $\log K_{zz} = 6$ match equally well and are far better than all other parameter combinations. For all four models from Table 2, the spectrum computed in chemical equilibrium ($K_{zz} = 0$) is by far the worst. Thus, the photometry strongly favors models that depart from chemical equilibrium.

For a fixed metallicity, the IRAC [4.5] flux is a sensitive probe of non-equilibrium carbon chemistry as the filter bandpass covers the fundamental band of CO centered at $4.65\,\mu\text{m}$. More vigorous vertical transport (i.e. larger K_{zz}) leads to an over-abundance of CO in the upper atmosphere and a strong band where none should be detectable at such low T_{eff} (Noll et al. 1997, Golimowski et al. 2004, Patten et al. 2006, Geballe et al. 2009). A low [4.5] flux is thus a hallmark of excess CO and of a non-equilibrium CO abundance. The observed [4.5] flux for Wolf 940 B is well below what would be expected from chemical equilibrium and only non-equilibrium models can match its value. We find that $\log K_{zz} = 5.5$ gives an excellent match and Figure 4 shows our best fitting non-equilibrium model spectrum, along with the corresponding equilibrium spectrum ($K_{zz} = 0$). A diffusion coefficient of $K_{zz} = 10^{5.5}\,\text{cm}^2\,\text{s}^{-1}$ corresponds to a vertical mixing time scale of ~ 4 hours. Note in Figure 4 the large difference

between the non-equilibrium and equilibrium models in [4.5] flux, and in the flux level in the $9 - 15 \mu\text{m}$ region where absorption by NH_3 dominates. Finally, we note that fitting K_{zz} independently from T_{eff} , gravity and L_{bol} affects L_{bol} by less than 0.016 dex, which is small compared to the contributions from the distance and flux calibration uncertainties of 0.047 dex.

4.5. Optimal Parameters for Solar Metallicity

Based on our solar metallicity model atmospheres, spectra and evolution, we conclude that Wolf 940 B is best fitted with $T_{\text{eff}} = 575 - 625 \text{ K}$, $\log g = 4.72 - 5.22$ and $\log K_{\text{zz}} \approx 5.5$. If we apply the age constraint of $3 - 10 \text{ Gyr}$ determined by the primary, then the parameter range is further restricted to $T_{\text{eff}} = 585 - 625 \text{ K}$ and $\log g = 4.83 - 5.22$. The derived parameters T_{eff} , $\log g$, K_{zz} , mass, radius and age are summarized in Table 3. As shown in Figure 2, the values of T_{eff} and $\log g$ are correlated, thus Wolf 940 B cannot be both low- T_{eff} and high gravity. These ranges do not reflect the effect of the uncertainty in the determination of L_{bol} of 0.047 dex, which translates to $\pm 16 \text{ K}$ in T_{eff} (for a fixed gravity) and ± 0.16 dex in gravity (for a fixed T_{eff}).

4.6. The Effects of Varying Distance and Metallicity

While we have been able to obtain a reasonably good fit of all the data available (parallax, spectra and photometry), systematic differences between the models and the near-infrared spectrum linger. In particular, we find that the models are much bluer in $J - K$ than the data (Figures 3 and 4). The K band modelled flux is about half of what is observed. A blue $J - K$ color in a late T dwarf is an indicator of a high-gravity or low-metallicity object (e.g. Knapp et al. 2004). Given all the constraints applied in our method of analysis, we cannot change the gravity independently of T_{eff} (except within the error bars) and we have seen that this has no effect on the K band flux (Figure 3). We can, however, consider variations in metallicity and of the distance, within the range allowed by the parallax uncertainty.

We have redone the complete analysis by assuming that the luminosity is increased by 1σ to $\log L_{\text{bol}}/L_{\odot} = -5.939$ (see Figure 2) and keeping $[\text{m}/\text{H}] = 0$. For consistency, this new luminosity implies that the distance is increased by 1.4σ to 13.58 pc. This moves our best fitting model of $T_{\text{eff}} = 600 \text{ K}$ and $\log g = 4.989$ to $T_{\text{eff}} = 625 \text{ K}$ and $\log g = 5.0$. This worsens the fit slightly, but well below the uncertainties and is thus not significant.

The analysis was performed again with model atmospheres, spectra and evolution of dif-

ferent metallicities. We find that a variation of $\Delta[m/H] = \pm 0.3$ results in $\log L_{\text{bol}} = \mp 0.023$, which is half of the uncertainty on L_{bol} due to the photometric and parallax uncertainties. Since the uncertainties in L_{bol} are effectively negligible in terms of spectrum fitting, for clarity of presentation we will make a comparison of spectra of different metallicity calculated with the best fitting $(T_{\text{eff}}, \log g) = (600, 5.0)$ we obtained in the solar metallicity case.

Spectra with $[m/H] = -0.3$ and $+0.3$ are shown in Figure 5. The optimal value of K_{zz} depends on $[m/H]$. To better show the role of $[m/H]$ in shaping the spectrum, we keep K_{zz} fixed at $10^4 \text{ cm}^2 \text{ s}^{-1}$ for the non-solar metallicity models. As expected, increasing the metallicity raises the modelled K band flux and a very good agreement is obtained for $[m/H] = +0.3$, but this comes at the cost of a significant increase in the modelled flux in the Y , J and H bands. On the other hand, the spectrum with $[m/H] = -0.3$ is an excellent match to the observed YJH peaks but increases the discrepancy at K . Calculation of the reduced χ^2 confirms the qualitative visual impression from the top panel of Figure 5 that the $[m/H] = -0.3$ spectrum is a better fit to the near infrared spectrum of Wolf 940 B. The lower panel shows the opposite situation at mid-infrared wavelengths: the fit of the spectrum improves steadily as the metallicity increases from -0.3 to $+0.3$. The mid-infrared photometry also favors higher metallicity if we neglect the poorly fit $3 - 4 \mu\text{m}$ region (where there is little flux). Hence varying the metallicity from $[m/H] = -0.3$ to $+0.3$ has a seesaw effect on the shape of the spectrum compared to the data and provides no real improvement over the solar metallicity fit. Since the extremes of that range lead to notably poor fits in the near-infrared or the mid-infrared, we can reasonably conclude that Wolf 940 B has a metallicity within ~ 0.2 dex of solar, which is consistent with the value of $[m/H] = +0.24 \pm 0.09$ derived for the primary star using the Johnson & Apps (2008) $M_K:V - K$ relationship (see §2).

Figure 5 (lower panel) shows that the $[4.5]$ flux is not only sensitive to K_{zz} , it is also sensitive to $[m/H]$. The best solar metallicity solution gives $\log K_{zz} \approx 5.5$ using this data-point, as described above in §4.4. If $[m/H] = +0.3$ then $\log K_{zz} \approx 4$ reproduces the observed $[4.5]$ flux, and similarly if $[m/H] = -0.3$ then $\log K_{zz} > 7$. Values of $\log K_{zz} = 4, 6$ and 7 correspond to mixing time scales of 2.8 days, 1.6 hours and 14 minutes respectively. The convective mixing time scale is 0.6 min for comparison, meaning that $\log K_{zz} > 7$ implies that mixing is almost as vigorous as convection which may not be realistic. A metallicity as low as $[m/H] = -0.3$ appears unlikely based on the very high value of K_{zz} required, again consistent with the solar or slightly metal-rich solution found for the primary.

5. Conclusions

We have presented a $7.5 - 14.2 \mu\text{m}$ low-resolution spectrum of the T8.5 dwarf Wolf 940 B, which is a companion to an M4 dwarf with a projected separation of 400 AU. This spectrum complements the near-infrared spectrum and L' photometry presented by B09, and the IRAC photometry presented by Leggett et al. (2010). Combining all these data allows a rigorous analysis of the dwarf’s SED. Assuming an age range of $3 - 10$ Gyr as indicated by the primary, evolutionary and atmospheric models show that for the T dwarf secondary $T_{\text{eff}} = 585 - 625 \text{ K}$ and $\log g = 4.83 - 5.22$. Gravity and temperature are correlated such that the lower gravity corresponds to the lower T_{eff} and younger age for the system, and the higher value to the higher T_{eff} and older age. The mass of the T dwarf is $24 M_{\text{Jupiter}}$ to $45 M_{\text{Jupiter}}$ for the younger to older age limits. An age younger than 1 Gyr is excluded by the analysis of the T dwarf spectrum alone.

These temperatures and gravities are slightly higher than those derived in B09. Our luminosity, which benefits from the inclusion of the IRS spectrum, is slightly (but not significantly) higher than determined by B09. Our higher temperature and gravity range principally arises from our more conservative approach to the age of the primary, for which we adopt $3 - 10$ Gyr as opposed to B09’s $3 - 5$ Gyr.

The IRS spectrum demonstrates that vertical mixing is important in the radiative zone of the atmosphere of Wolf 940 B, as is the case for many, if not all, T dwarfs. The $[4.5]$ photometric datapoint constrains $\log K_{zz}$ to 5.5 for solar metallicity. If the metallicity is higher then K_{zz} is lower, and vice versa. Comparison of the synthetic SED to the observational data shows that Wolf 940 B has a metallicity within ~ 0.2 dex of solar. More extreme values give poor fits to the data — lower metallicity produces a poor fit at $\lambda > 2 \mu\text{m}$ while higher metallicity produces a poor fit at $\lambda < 2 \mu\text{m}$. This is consistent with the value of $[\text{m}/\text{H}] = +0.24 \pm 0.09$ derived here for the primary star using the Johnson & Apps (2008) $M_K:V - K$ relationship.

It is very useful to find T dwarf companions to main sequence stars, given that the brown dwarfs are cooling and hence mass is difficult to constrain without knowing age. We look forward to more examples like Wolf 940 B (B09) and Ross 458 C (Goldman et al. 2010) being found, as the UKIDSS sky area increases.

This work is based on observations made with the *Spitzer Space Telescope*, which is operated by the Jet Propulsion Laboratory, California Institute of Technology under a contract with NASA. Support for this work was provided by NASA through an award issued by JPL/Caltech. Support for this work was also provided by the Spitzer Space Telescope

Theoretical Research Program, through NASA. SKL’s research is supported by the Gemini Observatory, which is operated by the Association of Universities for Research in Astronomy, Inc., on behalf of the international Gemini partnership of Argentina, Australia, Brazil, Canada, Chile, the United Kingdom, and the United States of America.

REFERENCES

- Biller, B. A., Kasper, M., Close, L. M., Brandner, W. & Kellner, S. 2006, *ApJ*, 641, L141
- Bonfils, X., Delfosse, X., Udry, S., Santos, N. C., Forveille, T. & Segransan, D. 2005, *A&A*, 442, 635
- Burgasser, A. J. et al. 2000, *ApJ*, 531 L57
- Burgasser, A. J., Kirkpatrick, J. D. & Lowrance, P. J. 2005, *AJ*, 29, 2849
- Burgasser, A. J. 2007, *ApJ*, 658, 617
- Burgasser, A. J., Tinney, C. G., Cushing, M. C., Saumon, D., Marley, M. S., Bennett, C. S. & Kirkpatrick, J. D. 2008, *ApJ*, 689, L53
- Burningham B. et al. 2008, *MNRAS*, 391, 320
- Burningham, B., et al. 2009, *MNRAS*, 395, 1237
- Burningham, B., et al. 2010, *MNRAS*, in press
- Burrows, A., Hubbard, W. B., Lunine, J. I. & Liebert, J. 2001, *Reviews of Modern Physics*, 73, 719
- Burrows, A., Sudarsky, D. & Lunine, J. I. 2003, *ApJ*, 596, 587
- Cutri, R. M. et al. 2003, *The IRSA 2MASS All-Sky Point Source Catalog*, NASA/IPAC Infrared Science Archive
- Dawson, P. C. & De Robertis, M. M. 2005, *PASP*, 117, 1
- Delorme P. et al. 2008a, *A&A*, 482, 961
- Delorme P. et al. 2008b, *A&A*, 484, 469
- Geballe, T. R., Saumon, D., Leggett, S.K., Knapp, G.R., Marley, M.S. & Lodders, K. 2001, *ApJ*, 556, 373

- Geballe, T. R., Saumon, D., Golimowski, D. A., Leggett, S. K., Marley, M. S. & Noll, K. S. 2009, *ApJ*, 695, 844
- Fazio, G. et al. 2004, *ApJS*, 154, 10
- Gizis, J. E., Reid, I. N. & Hawley, S. L. 2002, *AJ*, 123, 3356
- Goldman, B., Marsat, S., Henning, T., Clemens, C. & Greiner, J. 2010, *MNRAS*, in press
- Golimowski, D. A et al. 2004, *AJ*, 127, 3516
- Harrington, R. S. & Dahn, C. C. 1980, *AJ*, 85, 454
- Holmberg, J., Nordstrom, B. & Andersen, J. 2009, *A&A*, 501, 941
- Houck J. R. et al. 2004, *ApJS*, 154, 18
- Hubeny, I. & Burrows, A. 2007, *ApJ*, 669, 1248
- Johnson J. A. & Apps K. 2008, *ApJ*, 699, 933
- Kasper, M., Biller, B. A., Burrows, A., Brandner, W., Budaj, J. & Close, L. M. 2007, *A&A*, 471, 655
- Knapp, G. R. et al. 2004, *AJ*, 127, 3553
- Lawrence A. et al. 2007, *MNRAS*, 379, 1599
- Leggett, S. K., Hauschildt, P. H., Allard, F., Geballe, T. R. & Baron, E. 2002, *MNRAS*, 332, 78
- Leggett, S. K. et al. 2008, *ApJ*, 682, 1256
- Leggett, S. K. et al. 2009, *ApJ*, 695, 1517
- Leggett, S. K. et al. 2010, *ApJ*, 710, 1627
- Liu, M. C., Leggett, S. K. & Chiu, K. 2007, *ApJ*, 660, 1507
- Lucas, P. W. et al. 2010, *MNRAS*, in press
- Luhman, K. L. et al. 2007, *ApJ*, 654, 570
- McCaughrean M. J., Close, L. M., Scholz, R.-D., Lenzen, R., Biller, B., Brandner, W., Hartung, M. & Lodieu, N. 2004, *A&A*, 413, 1029

- Mermilliod J. C. 1997, VizieR On-line Data Catalog: II/168. Originally published in: Institut d’Astronomie, Universite de Lausanne (1991)
- Mugrauer, M., Seifahrt, A., Neuhauser, R. & Mazeh, T. 2006, MNRAS, 373, L31
- Nakajima, T., Oppenheimer, B. R., Kulkarni, S. R., Golimowski, D. A., Matthews, K. & Durrance, S. T. 1995, Nature, 378, 463
- Noll, K. S., Geballe, T. R. & Marley, M. S. 1997, ApJ, 489, L87
- Patten, B. M. et al. 2006, ApJ, 651, 502
- Reid, I. N., Hawley, S. L. & Gizis, J. E. 1995, AJ, 110, 1838
- Robin A. C., Reyle C., Derriere S. & Picaud S. 2003, A&A, 409, 523
- Saumon, D. & Marley, M. S. 2008, ApJ, in press.
- Saumon, D., Marley, M. S., Cushing, M.C., Leggett, S.K., Roellig, T.L., Lodders, K. & Freedman, R.S. 2006, ApJ, 647, 552
- Saumon, D., Marley, M. S., Leggett, S.K., Geballe, T.R., Stephens, D. S., Golimowski, D. A., Cushing, M. C., Fan, X., Rayner, J. T., Lodders, K. & Freedman, R. S. 2007, ApJ, 665, 1136
- Scholz R.-D., McCaughrean, M. J., Lodieu, N. & Kuhlbrodt, B. 2003, A&A, 398, L29
- Skrutskie M. F. et al. 2006, AJ, 131, 1163
- Smart, R. L. et al. 2010, aap, 511, 30
- Stephens, D. S., Leggett, S. K., Cushing, M. C., Saumon, D., Marley, M. S., Geballe T. R., Golimowski, D. A. & Fan, X. 2009, ApJ, 702, 154
- Tody, D. 1993, “IRAF in the Nineties” in Astronomical Data Analysis Software and Systems II, A.S.P. Conference Ser., Vol 52, eds. R.J. Hanisch, R.J.V. Brissenden, & J. Barnes, 173.
- Walkowicz, L. M. & Hawley, S. L. 2009, AJ, 137, 3297
- West, A. A. et al. 2008, AJ, 135, 785
- Wilson J. C., Kirkpatrick, J. D., Gizis, J. E., Skrutskie, M. F., Monet, D. G. & Houck, J. R. 2001, AJ, 122, 1989

York, D. G. et al. 2000, AJ, 120, 1579

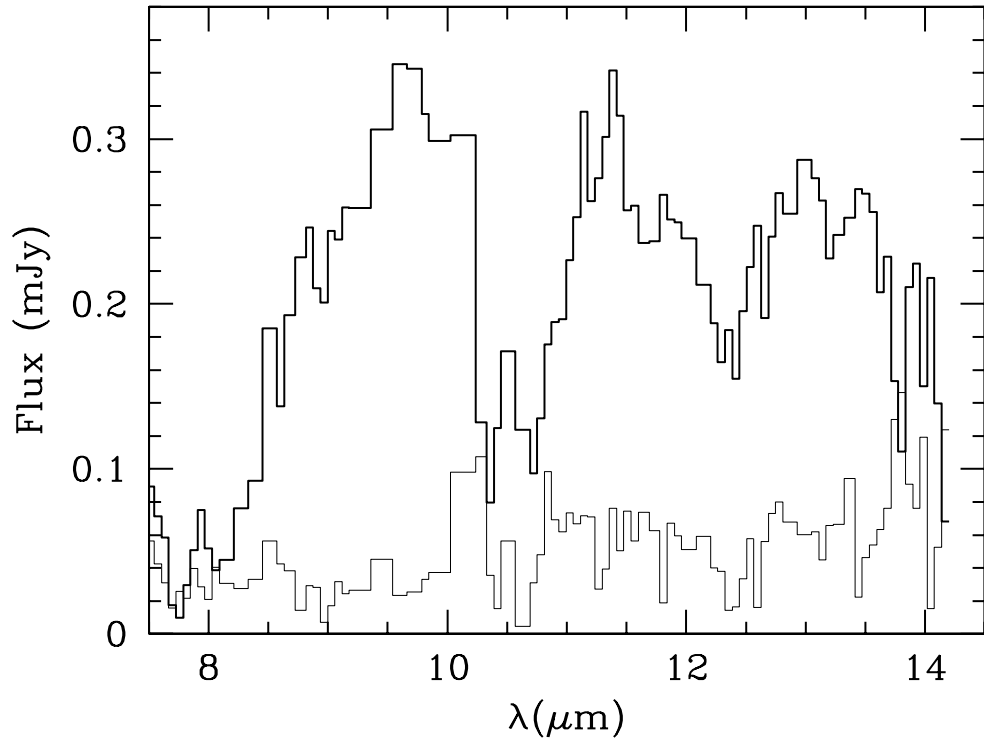


Fig. 1.— IRS spectrum of Wolf 940 B, the noise spectrum is shown in the lower region of the plot.

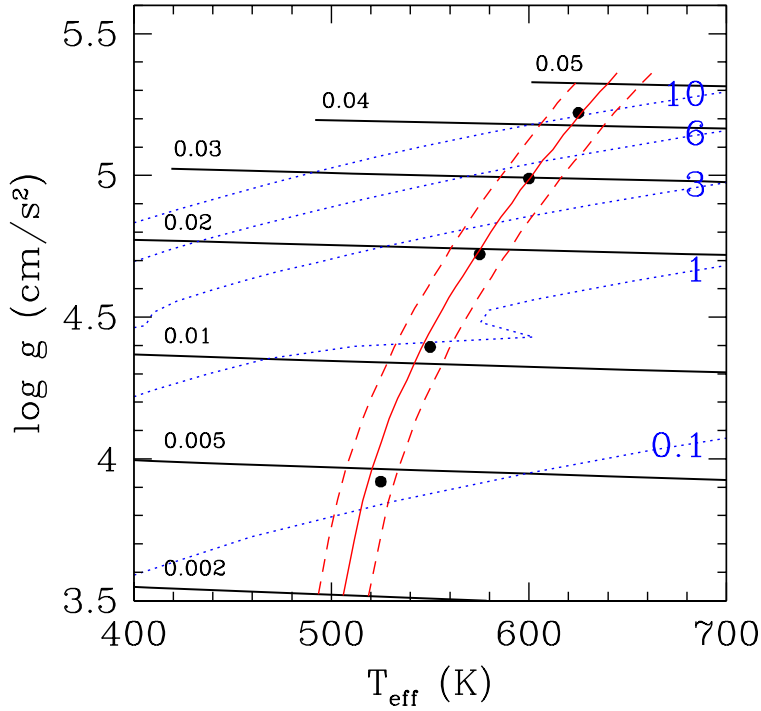


Fig. 2.— Evolution of cloudless brown dwarfs and constrained values of (T_{eff}, g) for Wolf 940 B. Brown dwarf cooling tracks (solid black lines) are labeled with the mass in M_{\odot} . Isochrones (blue dotted curves) are labeled with the age in Gyr. Solid dots are solutions for Wolf 940 B for $T_{\text{eff}} = 525$ to 625 K in steps of 25 K (see Table 2). A constant luminosity curve ($\log L_{\text{bol}}/L_{\odot} = -6.009$) is plotted to guide the eye (solid red curve), as well as its uncertainty ($\pm 0.047 \text{ dex}$, dashed red curves). We estimate the age of the Wolf 940 B system to be between 3 and 10 Gyr. The spur on the 1 Gyr isochrone is caused by deuterium burning.

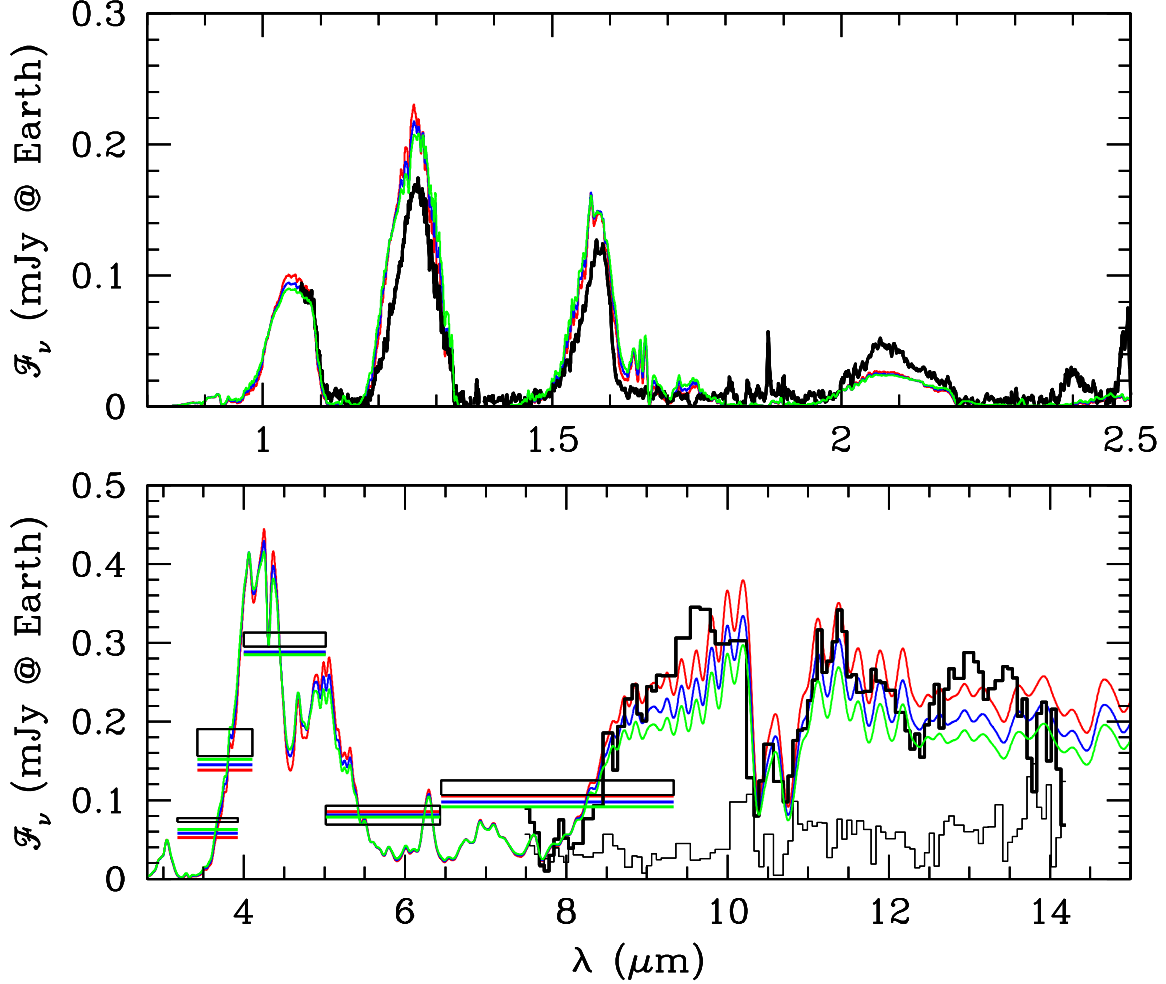


Fig. 3.— Model spectra corresponding to the constrained solutions for Wolf 940 B for $T_{\text{eff}} = 575$ K (red), 600 K (blue) and 625 K (green). See Figure 2 and Table 2. Photometric fluxes for these models are shown by horizontal lines. All fluxes are for cloudless models with an eddy diffusion coefficient of $\log K_{zz} = 6$ (see text) and are absolute, based on the measured distance and the radii given in Table 2. The data are shown in black, with photometric measurements shown as boxes with a height of $\pm 1\sigma$. For clarity, the near-infrared spectrum (B09, upper panel) has been smoothed with a running 7-pixel average. The IRS noise spectrum is shown in the lower panel.

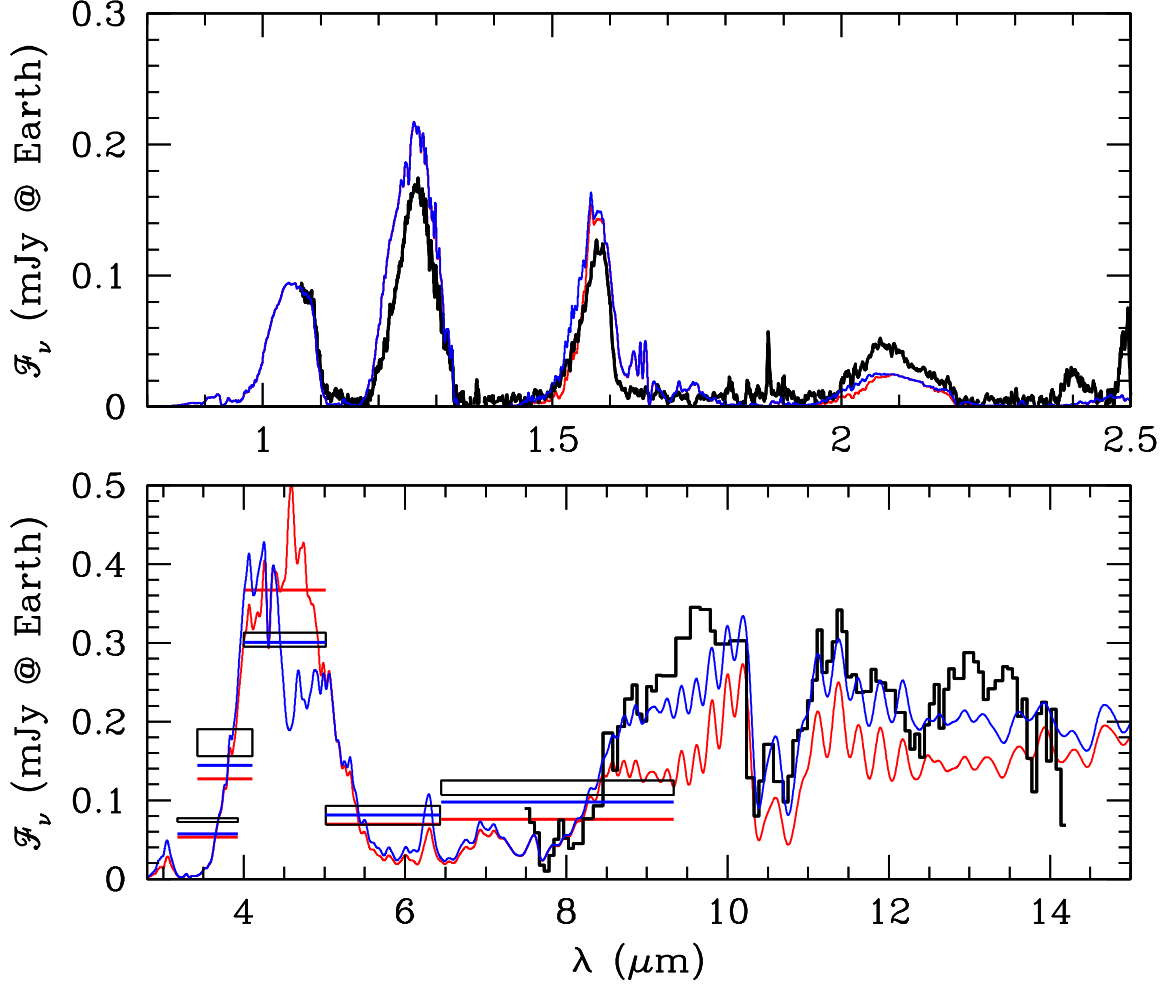


Fig. 4.— Best fitting model spectrum with solar metallicity ($T_{\text{eff}} = 600$ K, $\log g = 4.989$, $\log K_{zz} = 5.5$, blue curve) and the same spectrum computed with chemical equilibrium abundances ($K_{zz} = 0$, red curve). The large non-equilibrium abundance of CO is responsible for the strong band centered at $4.66 \mu\text{m}$. The reduced, non-equilibrium abundance of NH_3 results in a higher flux for $\lambda \gtrsim 8.5 \mu\text{m}$. See Figure 3 for additional details.

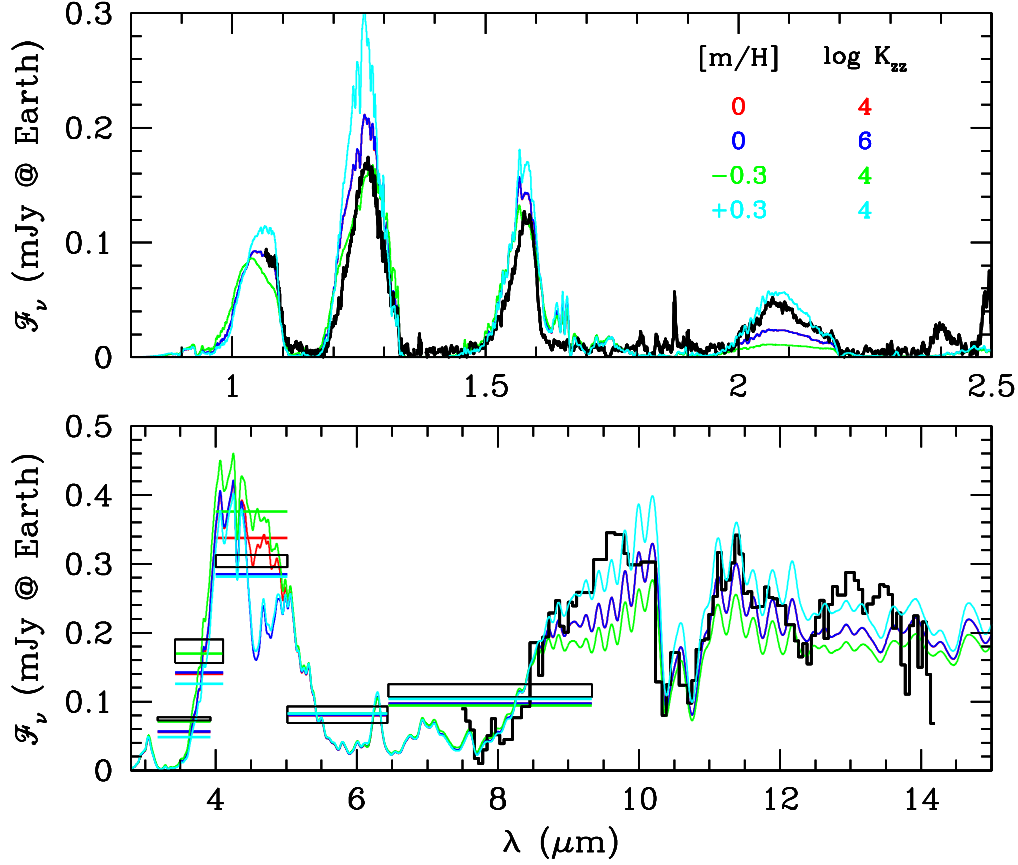


Fig. 5.— Effect of variations in the metallicity and eddy diffusion coefficient K_{zz} around the parameters of best fitting spectrum shown in Figure 4. All spectra shown have $T_{\text{eff}} = 600$ K and $\log g = 5$. The observed spectrum of Wolf 940 B is shown in black. Colored curves show spectra computed with the metallicity and eddy diffusion coefficients shown in the legend. The red and blue curves overlap everywhere except in the CO band centered at $4.6 \mu\text{m}$. The parameters of the model shown in blue are almost identical to those of the best fitting spectrum of Figure 4.

Table 1. Astrometric and Photometric Data for the Wolf 940 System

Property	Primary	Secondary
RA 2000, hhmmss.ss	21 46 40.47	21 46 38.41
Dec 2000, ddmms.s	-00 10 25.4	-00 10 34.6
Parallax mas	79.8 ± 4.5^a	...
PM RA mas yr ⁻¹	765 ± 2^a	...
PM Dec mas yr ⁻¹	-497 ± 2^a	...
Radial Vel. kms ⁻¹	-31.6 ± 12.2^b	...
Binary separation AU	400 ± 25^c	...
Binary PA deg.	253 ± 1^c	...
<i>V</i>	12.71 ± 0.06^d	...
<i>Y</i> MKO	...	18.97 ± 0.03^c
<i>J</i> 2MASS/MKO	8.36 ± 0.02^e	18.16 ± 0.02^c
<i>H</i> 2MASS/MKO	7.83 ± 0.03^e	18.77 ± 0.03^c
<i>Ks/K</i> 2MASS/MKO	7.49 ± 0.03^e	18.85 ± 0.05^c
<i>L'</i> MKO	...	15.38 ± 0.11^c
3.6 IRAC	...	16.44 ± 0.02^f
4.5 IRAC	...	14.43 ± 0.01^f
5.8 IRAC	...	15.38 ± 0.15^f
8.0 IRAC	...	14.36 ± 0.08^f

^aHarrington & Dahn 1980

^bDawson & De Robertis 2005

^cBurningham et al. 2009

^dMermilliod 1997

^e2MASS All-Sky Catalog of Point Sources, Cutri et al. 2003

^fLeggett et al. 2010

Table 2. Constrained Solutions to Wolf 940 B^a

T_{eff} (K)	$\log g$ (cm/s ²)	$\log L/L_{\odot}$	Mass (M _{Jupiter})	Radius (R _⊙)	Age (Gyr)
550	4.395	−5.994	12	0.1107	0.4
575	4.722	−6.004	20	0.1004	1.0
600	4.989	−6.009	31	0.0915	5.5
625	5.221	−6.012	45	0.0839	10

^aAssuming [m/H]=0.

Table 3. Final Adopted Parameter Set for Wolf 940 B^a

T_{eff} K	$\log g$	[m/H]	K_{zz} cm^2s^{-1}	Mass M_{Jupiter}	Radius R_{\odot}	Age Gyr
585 – 625	4.83 – 5.22	0.24 ± 0.09	$10^4\text{--}10^6$	24 – 45	0.097 – 0.084	3 – 10

^aTemperature, gravity, mass and radius are correlated and are listed in order of increasing age. Metallicity has been determined by application of the Johnson & Apps (2008) $M_K:V - K$ relationship to Wolf 940 A. Age is constrained by the kinematic and $\text{H}\alpha$ properties of Wolf 940 A.